



Investigation of the Impact of Thermo-Stamping, Fiber Orientation, and Metal Thickness on the Formability of Fiber Metal Laminates

Hamza Blala¹ · Cheng Pengzhi¹ · Zhang Shenglun^{1,2} · Cheng Gang¹ · Ruan Shangwen^{1,3} · Meng Zhang^{1,4}

Received: 16 April 2024 / Accepted: 26 June 2024 / Published online: 10 July 2024
© The Author(s), under exclusive licence to Springer Nature B.V. 2024

Abstract

Despite being invented several decades ago, fiber metal laminates (FMLs) still encounter challenges in large-scale manufacturing, especially in forming small and complex-shaped components. These challenges arise from the limited strain rate of the fiber layers compared to the metallic layers. Consequently, conventional approaches to form FML parts are often inadequate. To produce parts free of defects such as fractures and wrinkles, this study investigates the effects of Thermo-stamping (TH-S), in addition to fiber orientation, on the forming behavior of FMLs, employing two different aluminum layer thicknesses. A comprehensive approach combining finite element simulations and experimental analyses was employed. The study investigated thinning of aluminum alloy layers, stress distributions across different layers, and the influence of fiber orientation. The FML blanks are made of a middle woven glass fiber prepreg with a thickness of 0.2 mm, using a thermo-setting epoxy system, and Al 2024-T3 alloy sheets with varying thicknesses of 0.3 mm and 0.5 mm. Material behavior was evaluated using Abaqus software, applying the Johnson-Cook criterion for damage initiation in ductile metals and Hashin's theory for damage initiation in fiber-reinforced composites. These simulations were then compared with experimental results. The findings highlight the potential of the TH-S process to enhance the forming performance of FMLs, particularly evident in the case of the 0°/45° middle layer fiber, which exhibits a higher forming depth and a more uniform thickness distribution. Additionally, a greater flexibility of the glass fiber under the 0°/45° layup compared to the 0/90 layup was detected. This flexibility provides the aluminum layers with more freedom of deformation in the plastic domain. These advancements hold promise for widespread industrial applications of FMLs.

Keywords Fiber metal laminates (FMLs) · Thermo-stamping (TH-S) · Warm forming · Fracture · Drawing ratio

1 Introduction

FMLs were developed at Delft University of Technology in the early 1990s [1, 2]. This innovative material is made by alternating layers of metal sheets and fibers, subjected to specific temperature and pressure conditions for solidification. FMLs effectively combine the beneficial properties of metal materials with those of fiber-reinforced composites [3]. When compared to components made of equal volumes of metal alloy, FML components boast a remarkable reduction in mass by over 25%, while costing approximately one-third of their fiber-reinforced composite counterparts [4]. Moreover, FMLs exhibit outstanding properties such as high strength, fatigue resistance, and impact resistance [5, 6]. Autoclave forming, a conventional method employed for producing FMLs, relies on autoclave pressure to form large and small curved panels, such as aircraft fuselages. While this technique ensures a good product quality for large panels [7], it faces limitations when creating sharply curved small components due to inadequate gas pressure within the autoclave. Furthermore, the growth of autoclave forming processes is hindered by their high operational expenses and extended preparation times [8]. This prompted researchers to explore various manufacturing alternatives for producing small FML parts, including laser forming [9], incremental forming [10], and shot peening forming [11]. However, FMLs die-forming methods, including stamping, hydroforming, and bulging, have garnered the highest research focus [12, 13].

Several studies have investigated the forming ability of FMLs through stamping and hydroforming techniques. Consistently, researchers have found that employing rigid tooling for FML forming using conventional methods leads to several defects, including fractures, wrinkles, delamination, and insufficient forming depth. These defects are largely influenced by material properties such as fiber orientation and matrix viscosity, which play a crucial role in determining the failure mode of FMLs [14, 15], as well as affecting the deformation processes of the metal skin and the interfacial contact within the core layers [16, 17]. Warm forming emerges as a pivotal process, gaining increasing attention and exploration [18]. The utilization of elevated temperatures during the forming process “Thermoforming” not only influences the mechanical properties of individual layers but also imparts distinct advantages in terms of formability and overall performance [19, 20]. In 2005, Mosse et al. introduced a method involving pre-heating the FML to 160 °C before rapidly transferring it to the forming mold heated to 80 °C. After forming, the part is kept in the mold until solidification. The authors noted a significant improvements in shape error [21]. In 2007, Weiss et al. conducted further research on the impact of temperature on the forming behavior of an aluminum/PP/aluminum (APA) composite. Their findings indicated that forming at higher temperatures can effectively minimize springback. However, the decrease in strength of the core material as the process temperature rises resulted in laminate to wrinkle [22]. In 2015, Dou et al. proposed that elevated temperatures facilitate the flow of the matrix and enhance rotation at fiber strand intersections [23]. Additionally, in a study done by Zal et al. published in 2016, the authors examined the impact of layouts and forming temperatures on forming loads, spring back, fiber buckling, wrinkling, and delamination. FMLs were formed across temperatures ranging from 80 to 200 °C, and the results showed that delamination emerged as the primary defect in PVC-based FMLs, with successful forming at temperature of 160 °C [24]. Research attempt to improve the warm forming process, as the case presented by Nestler et al. Later in 2017, during warm forming of automobile FML at 250 °C. The authors used spacers for the tool gap, which lead to undefined pressure ratios in the FML

blank. The authors found that the gap varies as the temperature increases and the pressing force changes [25]. In 2018, Wollmann et al. examined FML comprising steel cover sheets and a carbon fiber-reinforced thermoplastic core. Heating both the blank and the tools to 230 °C, they found that forming of thermoplastic FMLs is feasible but restricted by wrinkling and cracking of metal cover, along with fiber failure, limiting the drawing depths [26]. In 2021, Wang et al. examined deeper the impacts of temperature and fiber direction on failures of FMLs. Their findings underscored the significant influence of fiber direction on failure mode and springback tendencies. Moreover, they highlighted the sensitivity of CFRP formability to temperature, with the springback rate differing by around 30% between room temperature and 150 °C. Additionally, the authors identified delamination between fiber and metal layers occurring at around 200 °C [27]. In 2021, Harhash et al. revealed that the thermoforming process allows for the processing of different FMLs material combinations and thicknesses. They found that increasing the core thickness and employing a 0/90 fiber orientation can enhance bending stiffness. However, the authors observed various defects, including delamination, plastic deformation, and fiber tearing, occurring through the forming operation [28]. In a recent study in 2022, Lu et al. investigated the manufacturing of curved Al/CF/PEEK beams using the hot stamp forming process. They discovered that by utilizing a forming temperature of 380 °C and a punching speed of 10 mm/s, they could produce curved beams with minimal spring-back of <math><0.2^\circ</math> and thickness reduction of <math><0.2\text{ mm}</math> [29]. Besides, in 2023, Harhash et al. experimental results revealed that warm forming could lead to over 300% improvement of the forming limit curve (FLC) of FML. However, other types of failure appear, such as wrinkling and core squeezing-out [30].

Traditional forming techniques often result in various defects when applied to FMLs, as highlighted in the literature. This emphasizes the need for deeper exploration into thermoforming processes for FMLs. In response to these challenges, this study investigates the innovative aspect of TH-S. By focusing on the production of cylindrical cups using 2/1 FMLs, we aim to unravel the intricate interplay between key parameters such as temperature, fiber orientation, and aluminum layer thickness. Through a comprehensive analysis, including numerical simulations and experimental data, our research seeks to understand the contributions of these factors to the formation of wrinkles, thinning, and overall formability of FMLs. By elucidating the synergistic effects and interactions among various input parameters, we aim to unlock new insights into optimizing FML manufacturing for mass production. By exploring thermoforming techniques, we aim to enhance the ability to produce small and complex-shaped parts with higher precision and fewer defects. Forming these small and complex FML parts is very limited with conventional techniques, making our research crucial for advancing the practical applications of FMLs in various industries, where the demand for intricate and reliable components is continually growing.

2 Experimental Setup

2.1 Materials and Sample Preparation

Aluminum alloy were used as a cover sheet for producing the FMLs blanks, namely the 2024-T3, from Kaiser Co. USA. The aluminum sheet were cut to a square shape of 140×140 mm with two different thickness of 0.3 and 0.5 mm. In the aerospace technology

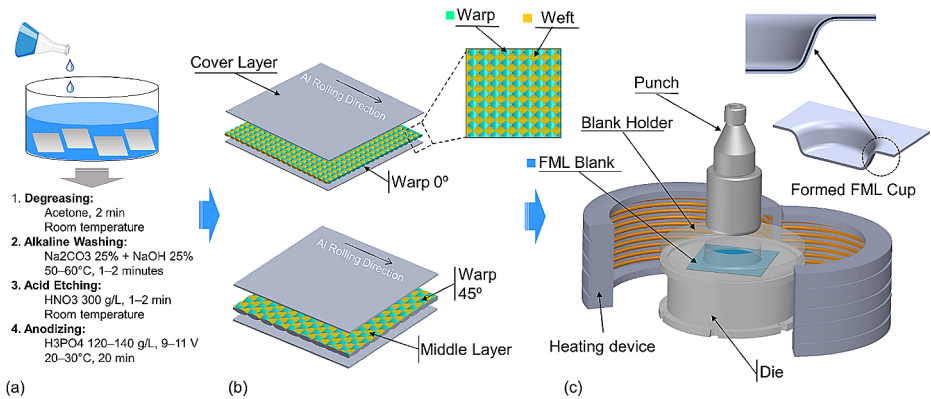


Fig. 1 Experiment set-up, **(a)** aluminum surface treatment, **(b)** 2/1 FMLs lay-up, **(c)** thermo-stamping mold

Table 1 2024-T3 alloy and the #218 prepreg mechanical properties [32]

2024-T3	Ultimate Tensile Strength (MPa)	Yield Strength at 0.2% (MPa)	Modulus of Elasticity (GPa)	Strain Hardening Exponent	Strength Index (MPa)	
	502	277	65	0.28	810	
#218 Prepreg	E_1 (GPa)	E_2 (GPa)	G_{12} (GPa)	X_t (MPa)	Y_t (MPa)	ν
	23	23	5.4	1213	1213	0.23

E_1 : Elastic modulus along the warp direction; E_2 : Elastic modulus along the weft direction; G_{12} : Shear modulus in-plane

X_t : Tensile strength along the warp direction; Y_t : Tensile strength along the weft direction; ν : Poisson’s ratio

sector, the requirements for composite material bonding quality are exceptionally strict. To meet these performance standards, surface pre-treatment involving phosphoric acid anodizing was conducted on the aluminum alloy sheets [31]. This process included vapor blasting with aluminum oxide, which roughened the surface to enhance the bonding agent’s adhesion to the prepreg (Fig. 1a). For the core materials, a plain woven glass fiber prepreg with a thermosetting epoxy system named #218, supplied by Guangwei Co., China, was used. The fiber weight is 204 g/m², and the resin content is 40%. The stacking sequence involved layering aluminum, the core material, and another layer of aluminum, as depicted in Fig. 1b. The aluminum blanks rolling direction was aligned with the fiber warp direction. The alignment was maintained consistently or adjusted to a 0°/45° as dictated by the particular experimental configuration. For the evaluation of tensile properties, ASTM E8 standards were adhered to for the 2024-T3 aluminum, while ASTM D-3039 standards were followed for the prepreg tests. The mechanical properties of these FML are presented in Table 1 [32].

The autoclave curing process is employed, with the temperature and pressure curves outlined in Fig. 2. The vacuum pump maintains a pressure of 0.1 MPa, which corresponds to a negative gauge pressure relative to atmospheric pressure, throughout the curing cycle. The temperature gradually increases from room temperature at a rate of 2 °C/min. Once reaching 80 °C, it is held for 30 min before continuing to rise at the same rate. Simultaneously, the air compressor injects compressed air up to 0.6 MPa, reaching a temperature of 135 °C for 90 min. Following heat preservation, the temperature decreases at a rate of 1 °C/min. When

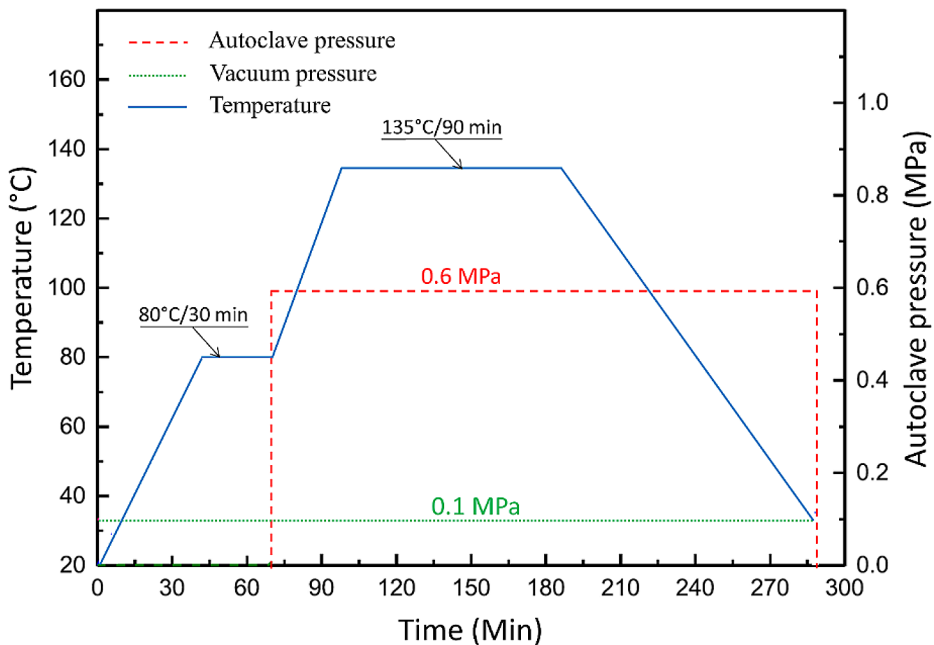


Fig. 2 The cure cycle for autoclave process of FMLs

it reaches 40 °C, the system is completed, the autoclave pressure is released, and the blank preparation process concludes.

2.2 Press Machine and Tools Dimensions

The FMLs thermo-stamping experiments were conducted using a 50-ton press machine to form a cylindrical cup with a diameter of 84 mm from a 140×140 mm square blank. The mold consisted of a die, punch, and blank-holder. The press is equipped with a heating device covering the die, holder, and punch head. Software connected to the hydraulic press allowed for monitoring of the experiment setup and measurements of drawing progress, including the blank holder force (BHF), punch load, punch speed, and temperature. The dimensions and assembly of the mold parts are depicted in Fig. 3.

3 Design of Experiments

In this study, we investigated the thermo-stamping performance of FMLs by considering three key process factors: stamping process (warm and room temperature stamping), fibers lay-up direction, and cover sheet layer thickness. Thermo-stamping was conducted at a temperature of 100 °C below the curing temperature of the thermoset resin. Standard experimental parameters were maintained, with the BHF set at 60 kN and a forming speed of 20 mm/min, and each experiment repeated three times under the same conditions. The experimental design based on the Taguchi method, is presented in Table 2.

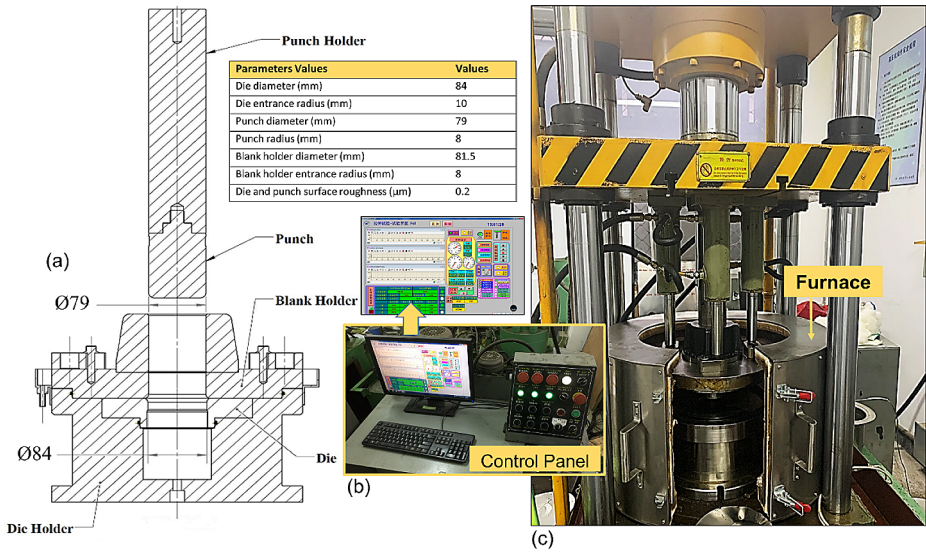


Fig. 3 Press Machine, (a) mold dimensions, (b) control panel, (c) hydraulic press

Table 2 Process factors experimental arrangement based on Taguchi L8 orthogonal array

Specimen N ^o	Process	Fibers orientation	Cover layer thickness (mm)
S1	TH-S	0/90	0.3
S2	TH-S	0/45	0.3
S3	TH-S	0/90	0.5
S4	TH-S	0/45	0.5
S5	RT-S	0/90	0.3
S6	RT-S	0/45	0.3
S7	RT-S	0/90	0.5
S8	RT-S	0/45	0.5

TH-S: Thermo-stamping
 RT-S: Room temperature stamping

4 Numerical Simulation

Finite element analysis (FEA) model in Abaqus software was employed to simulate the TH-S process for producing a cylindrical cup from a 2/1 FMLs laminate. The simulation setup for the FMLs laminate is illustrated in Fig. 4. The model consists of a punch, die, blank holder, and two layers of aluminum laminates sandwiching one layer of woven glass fiber in the middle. The elastic and plastic property data for aluminum are imported into the simulation. The Johnson-Cook criterion for damage initiation in ductile metals was integrated in the model. Hashin’s theory is used to determine the onset of damage in fiber reinforced composites [33]. The woven fiber was configured in both cross-ply orientations (0/90) and (0/45) in the composite section. To reduce calculation time, the punch, die, and blank holder were modeled as rigid components using a 3-D rigid quad-dominated element mesh with a mesh size of 3 mm. The die was fixed, while the punch and the blank holder

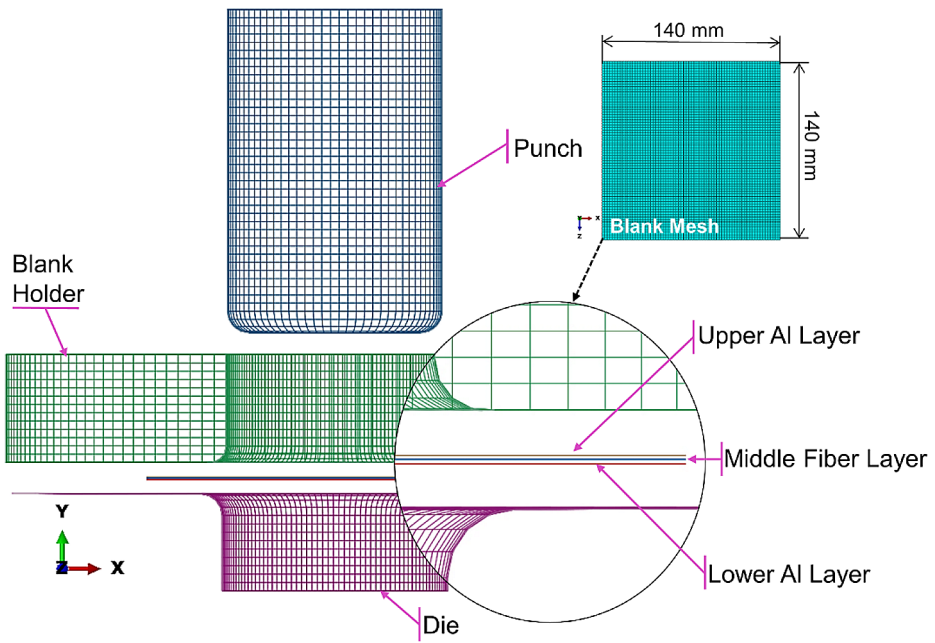


Fig. 4 FEA model setup

Table 3 Johnson Cook model parameters obtained for AL 2024-T3 alloy

A (MPa)	B (MPa)	<i>n</i>	C	m	$\dot{\epsilon}^*$ (s ⁻¹)	(ϵ)
277	684.5 MPa	0.34	0.002	1.0	1	0.2
<i>D</i> ₁	<i>D</i> ₂	<i>D</i> ₃	<i>D</i> ₄	<i>D</i> ₅	<i>T</i> _{melt}	σ^*
0.112	0.13	-1.5	0.007	0	509 °C	0.88

moves along the Y-axis with a constant blank holder force (BHF) of 60 kN. The 2/1 FML blank was considered a deformable body, meshed with a structured triangular mesh (S3R) with a mesh size of 2 mm. The simulation was conducted using a dynamic explicit step. The coefficient of friction between the aluminum layers and woven fiber prepreg layer is set at $\mu=0.5$ for the case of room temperature stamping [34]. Concerning the thermo-stamping predefined fields were activated with a constant temperature of 100 °C. Surface-to-surface contact is employed, with three tangential behaviors introduced for modeling the contacts: $\mu=0.15$ between the punch and upper sheet, $\mu=0.1$ between the blank holder and upper sheet, and $\mu=0.05$ between the lower sheet and die surface [35]. Additionally, an amplitude tool was integrated into the software.

4.1 Damage Model of FML Metal Cover

Damage assessment in the aluminum layers was conducted using the Johnson-Cook ductile damage model implemented in Abaqus (Table 3). The Johnson-Cook model incorporates the influence of strain, strain rate, and temperature on stress, making it widely applicable in

the engineering domain. This model comprises two components, the constitutive law and the failure criterion [36]. The effective stress is defined as:

$$\sigma = (A + B\epsilon^n) (1 + C \ln(\dot{\epsilon}^*)) (1 - T^{*m}) \quad (1)$$

Where A represents the yield stress, while B and n denote the parameters reflecting the strain hardening effect. These parameters are typically derived by fitting the plastic portion of the static tensile curves. C stands for the parameter governing the strain rate effect, where ϵ represents the equivalent plastic strain and; $\dot{\epsilon}^*$ signifies the normalized effective plastic strain rate. Additionally, m represents the thermal softening exponent, while T^* is a dimensionless temperature that can be determined through:

$$T^* = (T - T_r) / (T_m - T_r) \quad (2)$$

Where T_r represents the room temperature, while T_m is denotes the melting point of the material.

The Johnson-Cook model employs linear accumulation to account for the material's failure behavior throughout its deformation history. This method not only considers the variation of failure strain with stress state, strain rate, and temperature but also reflects the cumulative failure throughout the deformation process. The plastic failure strain ϵ_f is expressed as a function of stress state, strain rate, and temperature:

$$\epsilon_f = [D_1 + D_2 \exp(-D_3 \sigma^*)] [1 + D_4 \ln(\dot{\epsilon}^*)] [1 + D_5 T^*] \quad (3)$$

Here, σ^* represents the mean stress normalized by the effective stress, while D_1 - D_5 are failure parameters derived from experimental data. The damage parameter D reflects an accumulation value. Once this parameter reaches unity, damage to the metal component ensues. The determination of parameter D involves:

$$D = \sum \frac{\Delta \epsilon_{eq}}{\epsilon_f} \quad (4)$$

Where $\Delta \epsilon_{eq}$ represents the increment in equivalent plastic strain within an integration cycle.

4.2 Fiber Damage Initiation Criteria

Damage initiation indicates the beginning of degradation at a specific material point. In this damage model, initiation criteria are derived from Hashin's theory, where the failure surface is defined in the effective stress space. These criteria encompass four distinct damage initiation mechanisms: fiber tension, fiber compression, matrix tension, and matrix compression [37–39].

The initiation criteria have the following general forms:

Fiber tension ($\hat{\sigma}_{11} \geq 0$):

$$F_{ft} = \left(\frac{\hat{\sigma}_{11}}{X^T} \right)^2 + \alpha \left(\frac{\hat{\sigma}_{12}}{SL} \right)^2 = 1 \quad (5)$$

Fiber compression ($\hat{\sigma}_{11} < 0$) :

$$F_{fc} = \left(\frac{\hat{\sigma}_{11}}{X^C} \right)^2 = 1 \tag{6}$$

Matrix tension ($\hat{\sigma}_{22} \geq 0$) :

$$F_{mt} = \left(\frac{\hat{\sigma}_{22}}{Y^T} \right)^2 + \left(\frac{\hat{\sigma}_{12}}{S^L} \right)^2 = 1 \tag{7}$$

Matrix compression ($\hat{\sigma}_{22} < 0$) :

$$F_{mc} = \left(\frac{\hat{\sigma}_{22}}{2S^T} \right)^2 + \left[\left(\frac{Y^C}{2S^T} \right)^2 - 1 \right] \frac{\hat{\sigma}_{22}}{Y^C} + \left(\frac{\hat{\sigma}_{12}}{S^L} \right)^2 = 1 \tag{8}$$

In the equations above $\hat{\sigma}_{ij}$ represent the components of the effective stress tensor, while X^T and X^C signify the tensile and compressive strengths in the fiber direction, respectively. Similarly, Y^T and Y^C represent the tensile and compressive strengths in the matrix direction, and S^L and S^T denote the longitudinal and transverse shear strengths. The coefficient α in Eq. (5) dictates the contribution of the shear stress to the fiber tensile initiation criterion. Based on the value of this coefficient, the criteria can be specialized to obtain the model proposed in Hashin and Rotem [37] by setting $\alpha=0$ and $S^T = 0.5Y^C$ or the model proposed in Hashin [38] by setting $\alpha=1$.

5 Result and Discussion

5.1 Failure Mode and Forming Depth

Figure 5 depicts the fracture morphology resulting from FMLs cups formed under various experimental conditions. The stamping operation continued until the cup fractured to record the maximum achievable depth. In the experiments, the fracture criterion is based on monitoring the punch force during the forming process. The forming process is halted immediately following a significant drop in the punch force. This drop in force typically indicates

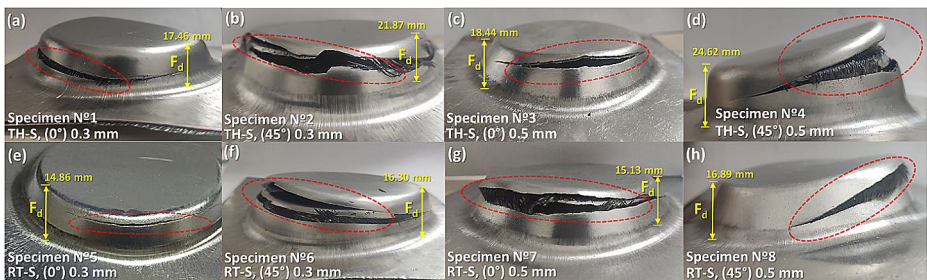


Fig. 5 Fracture morphology and forming depth (F_d) of the FMLs cups

the occurrence of fracture or failure within the specimen. Across all experimental specimens, fracture consistently occurred in the cup sidewall near the punch or near die corner.

Table 4 presents the results of forming depth and thinning values for the upper and lower cover layers under different experimental conditions. Analysis of Table 4 reveals that the chosen process factors of FMLs exhibit distinct effects, on forming depth and fracture characteristics. Furthermore, from the fracture patterns observed, it's evident that the fractures follow the fiber orientation of the middle layer, as illustrated in specimens 2, 4, 6, and 8 case of 0/45 fiber orientation. Fractures in specimens with a 0/90 fiber lay-up orientation appear linear, whereas those with a 0/45 orientation exhibit a woven appearance and varied directionality. This observation suggests that fiber orientation significantly influences fracture behavior in FMLs during stamping processes.

The initial thickness of the aluminum cover sheet has a marginal effect on increasing the forming depth of the laminate. For instance, under identical experimental conditions, the forming depth of the No.3 specimen (Initial thickness=0.5 mm) increased by 5.31% compared to the No.1 specimen (Initial thickness=0.3 mm), while that of No.4 specimen (Initial thickness=0.5 mm) increased by 11.16% compared to the No.2 specimen (Initial thickness=0.3 mm). However, under conventional RT-S conditions, the effect of aluminum layer thickness on forming depth is less pronounced. For example, the forming depth of the No.7 specimen (Initial thickness=0.5 mm) increased by only 1.78% compared to the No.5 specimen (Initial thickness=0.3 mm), and that of No.8 specimen (Initial thickness=0.5 mm) increased by 3.49% compared to the No.6 specimen (Initial thickness=0.3 mm). This suggests that while aluminum layer thickness does influence forming depth to some extent, other factors may play a more dominant role under specific experimental conditions.

The fiber orientation within the middle layer plays a pivotal role in improving the forming depth of the laminate. Under identical experimental conditions, the forming depth of specimen No.2 (0/45) increased by 20.16% compared to specimen No.1 (0/90), and that of specimen No.4 (0/45) increased by 25.10% compared to specimen No.3 (0/90). Under conventional RT-S, the forming depth of specimen No. 6 (0/45) increased by 8.83% compared to specimen No.5 (0/90), and the depth of specimen No.8 (0/45) increased by 10.42% compared to specimen No.7 (0/90). The arrangement of fibers in the 0/45 direction emerges

Table 4 Experiments and simulation results evaluation

N°	Fiber fracture initiation At depth Sim. (mm)	Forming Depth At fracture Exp. (mm) (SD)	Al Thinning			
			Simulation values		Experimental values	
			Upper layer (mm)	Lower layer (mm)	Upper layer (mm) (SD)	Lower layer (mm) (SD)
S1	15.30	17.49 (±0.57)	0.288	0.287	0.2917 (±0.0300)	0.2890 (±0.0251)
S2	18.12	21.75 (±0.40)	0.289	0.287	0.2850 (±0.0200)	0.2680 (±0.0113)
S3	16.80	18.71 (±0.23)	0.479	0.485	0.4333 (±0.0451)	0.4710 (±0.0101)
S4	19.48	24.57 (±0.40)	0.472	0.472	0.4507 (±0.0272)	0.4703 (±0.0055)
S5	12.16	14.89 (±0.40)	0.285	0.285	0.2867 (±0.0247)	0.3007 (±0.0253)
S6	14.08	16.57 (±0.36)	0.283	0.283	0.2757 (±0.0190)	0.2710 (±0.0295)
S7	13.14	15.31 (±0.33)	0.480	0.480	0.4143 (±0.0561)	0.4473 (±0.0064)
S8	14.40	16.93 (±0.25)	0.470	0.472	0.4233 (±0.0252)	0.4513 (±0.0055)

SD: Standard Deviation

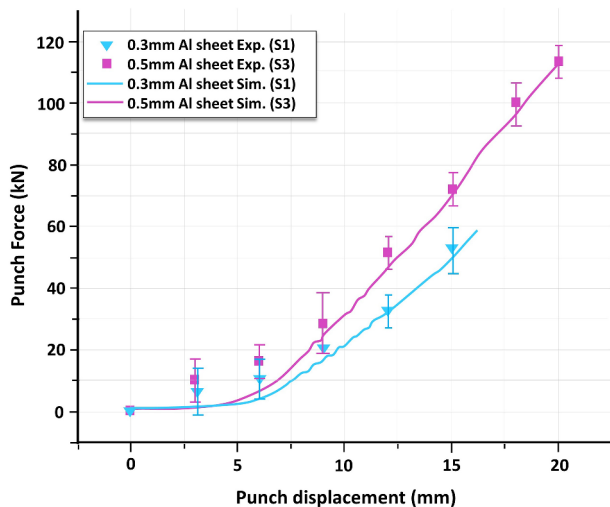
as advantageous for increasing the forming limit. In the 0/45 fiber layup, fibers are aligned at 0° and 0/45 relative to the axis, offering a strategic arrangement that contributes to superior forming performance. This configuration facilitates more effective stress distribution during the forming process, thereby reducing the likelihood of premature failure and enhancing the overall formability of the material. Moreover, the 0/45 fiber direction provides enhanced resistance against fractures and promotes more uniform deformation across the material, resulting in increased forming depth compared to 0/90 fiber orientations. Consequently, the 0/45 fiber direction in FMLs proves to be a beneficial choice for optimizing forming depth. Its ability to efficiently distribute stress and enhance the material's overall formability leads to improved performance in forming processes, underscoring its significance in FML manufacturing and design considerations.

The thermo-stamping process proves to be very effective in enhancing the forming depth of the laminate. Similarly, under identical experimental conditions, the forming depth of specimen No.1 (100 °C) increased by 14.89% compared to specimen No. 5 formed by RT-S, and that of specimen No.2 (100 °C) increased by 25.46% compared to specimen No.6 formed by RT-S. Additionally, the forming depth of specimen No.3 (100 °C) increased by 17.95% compared to specimen No.7, and that of specimen No. 4 (100 °C) increased by 31.39% compared to specimen No.8 formed by RT-S. From these results, TH-S proves to be the most influential factor, followed by fiber orientation and cover layer thickness.

5.2 Process Interaction with the Punch Force

This segment primarily discusses the impact of selected factors on the punch force, including fiber orientation, thickness of the aluminum alloy cover layer, and forming temperature. Figure 6 presents a comparison between simulation and experimental results of the punch force-displacement during forming FML by varying thicknesses of the aluminum cover. It is evident that punch force of the laminate with a 0.5 mm aluminum cove thickness is much higher compared to FMLs with a cover layer thickness of 0.3 mm. The maximum forming force increased by 37.2% for the 0.5 mm cover sheet thickness compared to that of FMLs with a 0.3 mm cover sheet thickness. Additionally, the two curves diverge in the initial sec-

Fig. 6 Comparison of punch force and displacement curves as a function of cover layer thickness (Specimens S1 and S3)



tion, indicating that the required punch force for forming FMLs with thicker outer layers is consistently greater than that of FMLs with thinner aluminum cover. The experimental findings align with the simulation results. However, a notable discrepancy between simulation and experimental results is observed in the initial stage of the curve, attributed to nonlinear changes in contact friction of the FML layers at the onset of forming. Nevertheless, the final stage error margin stands at approximately 3.4%, affirming the reliability of simulation results. This underscores the importance of accurately predicting punch force in FML forming processes for efficient machine sizing and reliable engineering design.

Figure 7 provides insights into the impact of fiber lay-up orientation on punch force. The punch force exhibited a slight increase under the 0/45 fiber lay-up compared to the 0/90 direction. The difference between these two conditions was found to be less than 4%. This observed phenomenon can be attributed to the advantageous nature of the 0/45 fiber orientation in FMLs. This particular orientation proves more effective in shifting the load from the external aluminum cover to the middle prepreg layer when compared to the 0/90 fiber lay-up. The middle fiber at 0/45 facilitates a more efficient load transfer mechanism, resulting in a slightly larger punch force. Moreover, the inherent characteristics of the fibers, including their stiffness and strength, play a crucial role in this behavior. The middle fibers in the 0/45 direction exhibit significantly greater stiffness and strength than aluminum. Consequently, the punch force experienced by the FML with 0/45 orientation is larger, underscoring the influence of lay-up direction on the mechanical performance of FMLs.

Figure 8 illustrates the punch force-displacement relationship and the impact of forming temperature on the punch force. The curves remained closely aligned until a punch displacement of 13 mm, after which a noticeable deviation occurred beyond 15 mm. A comparison was made regarding the maximum punch force at a forming depth of 20 mm. It was observed that the punch force slightly decreased during thermos-stamping compared to room temperature stamping. This trend was consistent between experimental and simulation results, as depicted in Fig. 8. The disparity in punch force can be attributed to differing contact conditions during RT-S and TH-S. The decrease in resin viscosity due to temperature contributes to the reduction in punch force. During forming at room temperature the prepreg exhibits stronger bonding performance, transmitting the forming force across the

Fig. 7 Punch force versus displacement curves as a function of fiber orientation (Specimens S7 and S8)

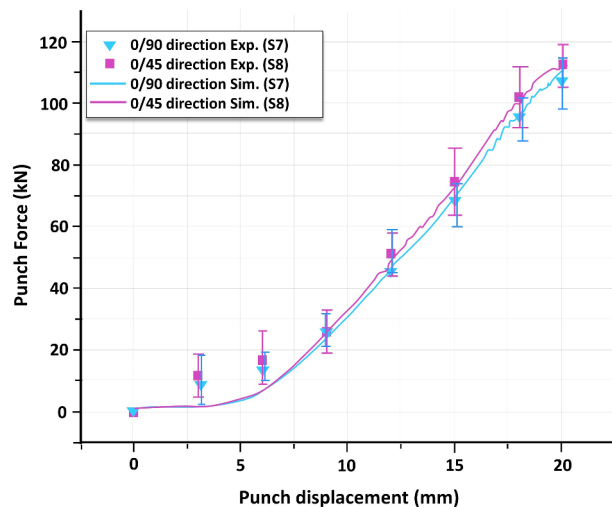


Fig. 8 Comparison of the punch force and displacement curves as a function of temperature (Specimens S4 and S8)

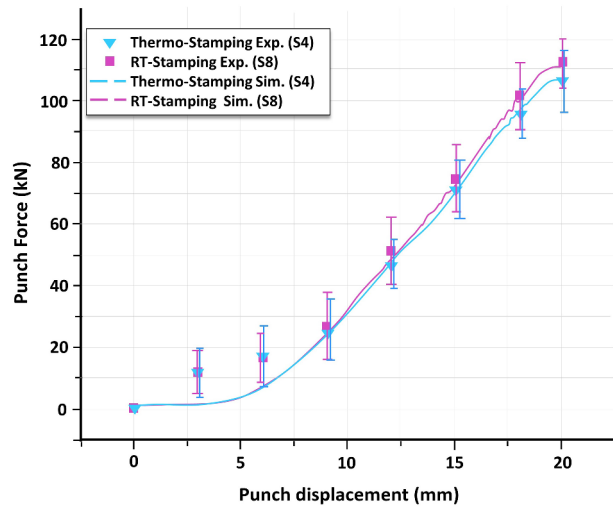


Fig. 9 FML cup cutting direction for wall thickness measurements

FML layers, and the fibers bears a greater portion of the load. Comparing simulation results with experimental data reveals a close alignment, indicating the predictability of maximum punch force and offering insights for selecting stamping process parameters.

5.3 Process Interaction with the FML Thickness

Analyzing of the wall thickness distribution is an important step to evaluate the formed FMLs quality and to understand the effect of each selected factors. As shown in Fig. 9 the formed laminates parts cut at two directions 0° and 45° to measure the maximum wall thickness reduction of each specimen.

The FMLs cups wall thickness is represented in Table 4, and the following Fig. 10. From the results the predicted thinning using simulation analysis was closely related to the experimental values, but also we can see some difference which we believe is due to the surface friction coefficient variation. In all specimens the maximum thinning region, occurs on the punch summit area, At 30 and 110 mm distance along the formed cup the wall thickness is quite smaller, it means that these two points are in such a position in the sheet where a

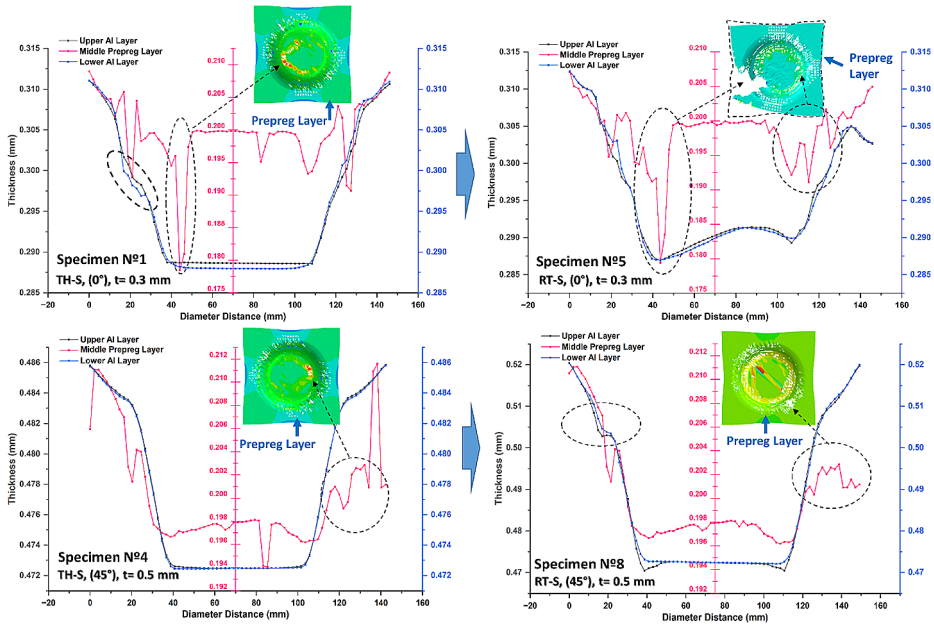


Fig. 10 Specimens S1, S4, S5 and S8 wall thickness comparison

combined effect of tensile and bending stress leads to a maximum thinning at these points. To analyze the effect of the initial thickness of the aluminum cover on the wall thickness reduction, specimens S1 and S3 were used for comparison under the same forming conditions (TH-S process and 0/90 fiber layout). Specimen S1, with an initial aluminum thickness of 0.3 mm, showed a thinning value of 5.66% for the upper aluminum layer and 4.33% for the lower aluminum layer, while specimen S3, with an initial aluminum thickness of 0.5 mm, reached a wall thickness reduction of 4% for the upper aluminum layer and 5.4% for the lower aluminum layer. Under the same forming conditions (TH-S process and 0/45 fiber layout). Specimen S2, with an initial thickness of 0.3 mm, exhibited a thinning of 5% for the upper aluminum layer and 8.66% for the lower aluminum layer, while S4, with an initial thickness of 0.5 mm, recorded a reduction in thickness of 9.6% for the upper aluminum layer and 11% for the lower aluminum layer.

In the case of the RT-S process, specimens S5 and S7 were compared with specimens S6 and S8 under the same forming conditions. The RT-S experiments revealed that the upper aluminum layer of the S5 sample experienced 8.33% thinning, and 9.33% for the lower aluminum layer, while the S7 sample showed a 9.4% reduction in thickness for the upper aluminum layer, and 9.6% for the lower aluminum layer. The thickness reduction for S6 was recorded to be 14.33% for the upper aluminum layer and 15.66% for the lower aluminum layer, while S8 exhibited a thinning rate of 11.6% for the upper aluminum layer, and 12% for the lower aluminum layer. These results indicate that the initial thickness had a lesser effect on the wall thickness reduction in the case of TH-S, with a maximum thinning rate of 5.66%. However, in the case of RT-S, the thinning rate increased, reaching 15.66% for sample S6. Nevertheless, these thinning values still fall within the range of elongation at break for the aluminum alloy 2024-T3, which is 18%.

Regarding fiber orientation, the results show that fiber layup has an impact on the wall thickness of FMLs. Specimen S1 with (0/90) fiber orientation exhibited an upper aluminum thinning of (5.66%) and a lower aluminum thinning of (4.33%), while specimen S2 with (0/45) fiber layup showed an increase in wall thinning by (5%) for the upper layer and (8.66%) for the lower layer. Similarly, all specimens exhibited the effect of the 0/45 layup on increasing the thinning rate of the cover layers. For instance, in S3 with (0/90) fiber orientation, the thinning rates for the upper and lower aluminum layers were (4%) and (5.4%), respectively, whereas in S4 with (0/45) fiber orientation, the thinning rates were (9.6%) and (11%), respectively. Furthermore, in S5 with (0/90) fiber orientation, the thinning rates for the upper and lower aluminum layers were (8.33%) and (9.33%), respectively, while in S6 with (0/45) fiber orientation, the thinning rates increased to (14.33%) and (15.66%), respectively. Similarly, for S7, with (0/90) fiber layup, the thinning rates for the upper and lower aluminum layers were (9.4%) and (9.6%), respectively, while in S8, under (0/45) layup, the thinning rates increased to (11.6%) and (12%) for the upper and lower layers, respectively. This can be explained by the relatively large deformation of the glass fiber under the 0/45 layup compared to the 0/90 layup, which allows the aluminum layers more freedom of deformation in the plastic domain.

The TH-S process has proven to have a significant effect on wall thickness reduction. Specimen S1 under TH-S showed less thinning compared to the RT-S process. The upper aluminum thinning was 5.66%, and the lower aluminum layer reached 4.33%, whereas for specimen S5 with RT-S process, the thinning rates for the upper and lower aluminum layers were 8.33% and 9.33%, respectively. Specimen S2 under TH-S exhibited a wall thinning of 5% for the upper layer and 8.66% for the lower layer. In comparison, specimen S6, formed at room temperature, experienced an increased thinning rate of 14.33% for the upper layer and 15.66% for the lower layer. Furthermore, specimen S3 formed using the TH-S process exhibited thinning rates of 4% and 5.4% for the upper and lower aluminum layers, respectively, while specimen S7, formed using the conventional process, showed an increased thinning rate of 9.4% for the upper layer and 9.6% for the lower layer. Another comparison between specimens S4 and S8 revealed that in S4, formed using the TH-S process, the thinning rates for the upper and lower aluminum layers were 9.6% and 11%, respectively, while in S8, formed using the RT-S process, the thinning rates showed an increase of 11.6% for the upper layer and 12% for the lower layer. This can be explained in light of the reduction in interlayer friction due to the temperature factor, which improves the formability of FMLs. The TH-S process involves the application of both heat and pressure during forming. This combination facilitates better material flow and distribution, resulting in more uniform deformation across the FML structure. By subjecting the material to elevated temperatures, the viscosity of the resin matrix is lowered, allowing for easier deformation and reduced interlayer friction. Consequently, this promotes smoother material flow and minimizes localized thinning, as evidenced by the lower thinning rates observed in specimens formed under TH-S conditions. In Fig. 10, a comparison is presented between specimens No.1 and No.5, as well as between No.4 and No.8. It is evident that the curves of the 0/45 fiber layup exhibit uniformity and good alignment, unlike those of the 0/90 lay-up. Additionally, fiber damage can be observed in the thinning curve, manifesting as a deviation drop in the thickness.

5.4 Interaction with Stress-Strain Distribution

In all specimens, the maximum logarithmic strains were located in the area of the punch corner, cup wall, and die corner. The failure of the aluminum layers occurs immediately after fiber breakage. Wrinkles are more likely to occur when using the TH-S process, as shown in specimens 1, 2, and 3 due to the decrease in resin viscosity under the stamping temperature. However, it should be noted that these wrinkles were recorded with very small amplitudes in the experiments and can be eliminated by adjusting the BHF. According to the simulation results, the maximum logarithmic strain varies with the thickness of the aluminum layers, as shown in Fig. 11. The maximum strains were observed to be higher with 0.5 mm of aluminum thickness than with 0.3 mm. The aluminum cover with 0.5 mm exhibits higher stiffness and resistance to deformation. As a result, it requires more force and energy to undergo the same amount of deformation as the thinner aluminum blank. Furthermore, 0.5 mm of aluminum thickness experiences higher strains during deformation compared to thinner aluminum layers under the same forming conditions. This increased strain results in higher strain energy, which contributes to elevated stress levels within the material. Regarding the deformation patterns of the FML blank, the corners of the square blank experience more significant deformation than the edges. This non-uniform deformation lead to the creation of a floral pattern, with the corners forming petals.

Figure 12 depict the evolution of fiber failure throughout the stamping process of specimens 2, 5, 7 and 8. The simulation results concerning the progression of fiber tensile and shear damage modes are outlined below. It is evident that multiple failure modes emerge on the composite laminate during the entire forming process. The process of damage propagation can be categorized into three stages based on the rate of progression. Firstly, there is a phase characterized by slow damage development. This is attributed to the robust mechanical properties of the fiber prepreg and the relative movement of fibers within the laminate during TH-S. However, this stage is brief due to the sharp decline in the load-bearing capacity of the FML upon the occurrence of fiber damage. Secondly, there is a phase marked by rapid damage escalation. The force exerted by the punch travel accelerates the spread of each damage mode during this stage, with matrix tensile damage exhibiting the highest propagation rate. Additionally, the results indicate that FMLs with a 0/45 fiber orientation exhibit more uniform deformation compared to those with a 0° fiber orientation, as evidenced by cases S2 and S8. The fracture locations predicted by the simulation models closely align with the experimental results. Fiber damage represented by elements dilatation was predominantly situated adjacent to the punch and die corners, while other areas remained undamaged. Notably, in cases of 0/90 fiber orientation, fiber damage was more severe compared to 0/45 fiber orientation, consistent with the fracture morphologies observed in specimens S5 and S7 in Fig. 12.

Figure 13 display formed FML cups and distribution of maximum principal stress from the specimens S1, S4, and S6 experiment. The figure illustrate the experimental fracture locations in comparison to the stress distribution found by simulation. It can be observed the FMLs cup fracture occurred at the punch and die corner. This location presents a significant risk for forming failure because of the sharp corner, and the fiber with 0/45 lay-up can only carry a limited load causing the aluminum to bear a large amount of stress. This finding align with the examination on the impact on punch force and its influence on the distribution of wall thickness and stress-strain profiles. Concerning cases S4, which is thermos-stamped

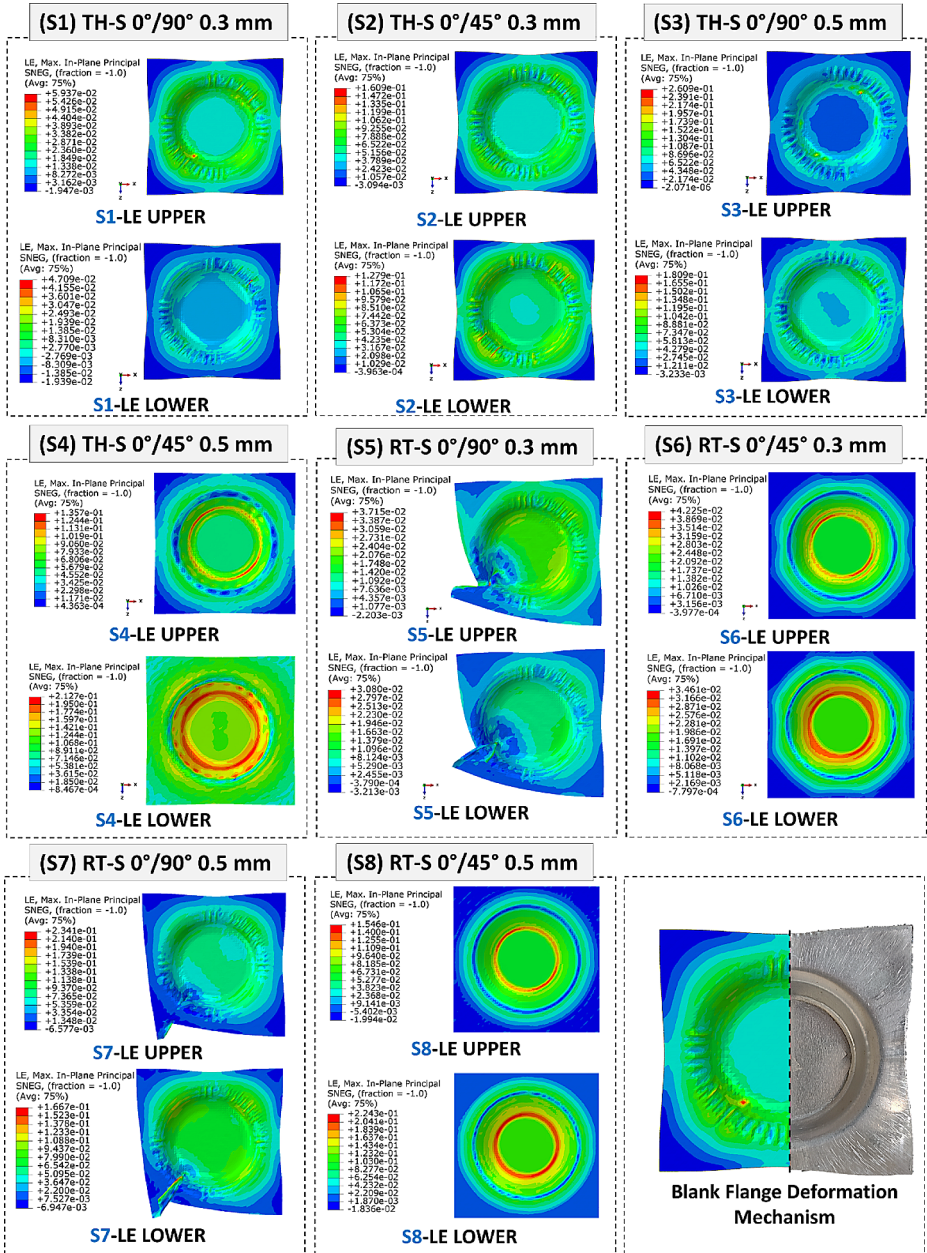
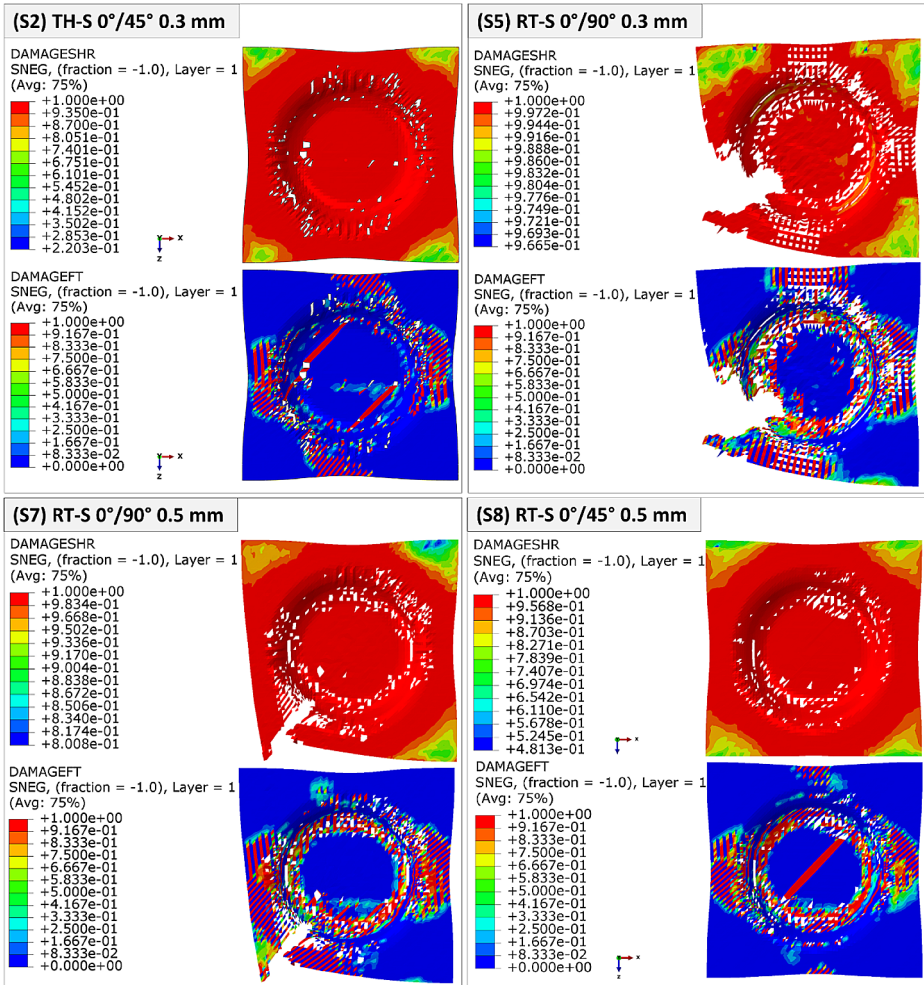


Fig. 11 Maximum logarithmic strain of the aluminum layers, and deformation patterns

FML, reach a forming depth of 24.62 with an improvement of 31.39%, the stress transition exhibited better uniformity and efficiency, enabling the transmission of forming stress to the external aluminum sheets, as in Fig. 13. Not that the forming was until the cup fracture to record the maximum forming depth and fracture location.



DAMAGEFT: Fiber tensile damage variable. **DAMAGESHR:** Shear damage variable.

Fig. 12 Fiber damage comparison of Specimens S2-S8 (0/45) and S5-S7 (0/90)

To examine the morphology of the formed fiberglass layer, the aluminum component was extracted from the FML cup, as illustrated in Fig. 14. The figure emphasizes the primary directions of stress-bearing of the fiber cloth through red arrows. The weave pattern of the fiber results in distinct force distributions along these specified directions. Upon closer examination in the enlarged images, it becomes apparent that the fiber predominantly carries the load along its direction at 0°, whereas fiber torsion significantly contributes to load-bearing at 45°. Fiber torsion refers to the rotational movement between two fiber bundles in their relative positions. Despite the considerable deformation range of the fiber layer, the load it experiences remains relatively minimal. Importantly, the load at this point effectively transfers to the external aluminum sheets, leading to fractures occurring in the cup wall and at the punch radii.

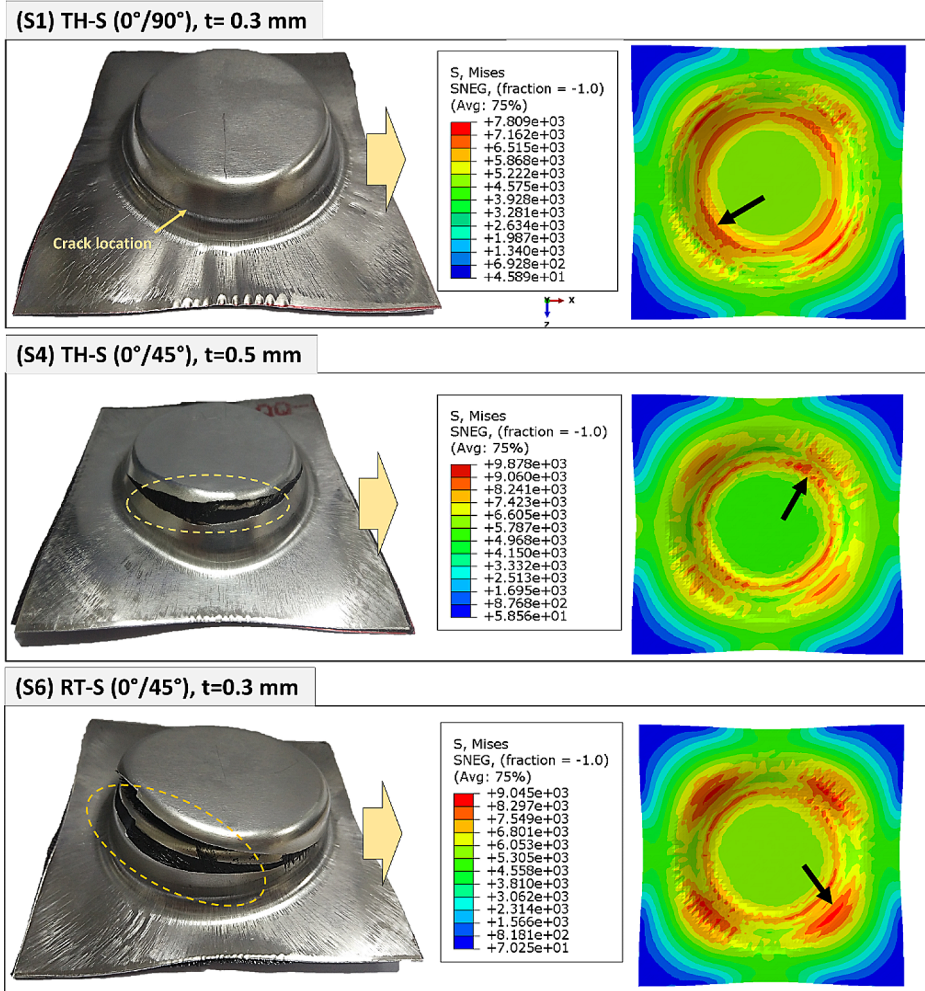


Fig. 13 Experiment and simulation comparison between stress concentration in MPa, and fracture location

6 Conclusion

In this study, the aim was to enhance the formability of Fiber Metal Laminates (FMLs) and produce defect-free parts. To achieve this, the thermo-stamping (TH-S) process was thoroughly investigated, along with considerations of fiber orientation and cover layer thickness. The findings of this investigation lead to several key conclusions. Firstly, the thermo-stamping process has been shown to significantly enhance the forming performance of FMLs, particularly evident in the case of the 0/45 middle layer fiber, which exhibits a higher forming depth. Secondly, FMLs with a 0.5 mm external aluminum layer, subjected to TH-S with a 0/45 middle layer orientation, demonstrate the highest forming load, with simulation results closely matching experimental findings—the maximum simulated punch force deviating by less than 4%. Additionally, a large flexibility of the glass fiber under the

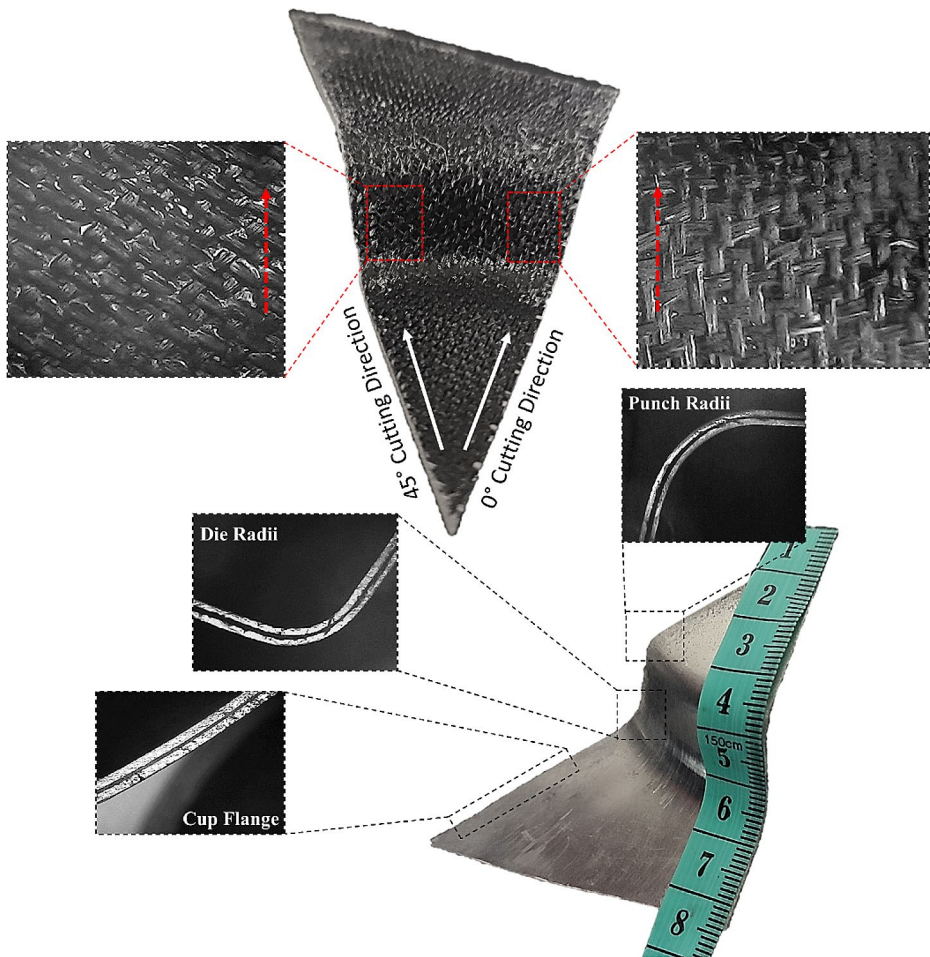


Fig. 14 The woven fiber morphology within the middle layer of the S4 experimental specimen

0/45 layup compared to the 0/90 layup was detected. This flexibility provides the aluminum layers with more freedom of deformation in the plastic domain. Lastly, compared to conventional stamping, TH-S with a 0/45 middle fiber layer orientation promotes a more uniform distribution of thickness in the outer aluminum layers. This effect is attributed to a certain degree of interlayer slip, which helps mitigate excessive fiber deformation, ultimately increasing the forming depth of the FMLs. Based on these findings future research could explore a wider range of materials, fiber orientations, and process parameters to enhance the robustness and applicability of the results.

Author Contributions Hamza Blala: Conceptualization, Investigation, Methodology, Writing - original draft. Cheng Pengzhi: Supervision, Project administration, Funding acquisition, Validation. Zhang Shenglun: Visualization, Data curation, Writing - Review & Editing. Cheng Gang: Supervision, Writing- Reviewing and Editing. Ruan Shangwen: Formal analysis, Review. Meng Zhang: Data curation, Investigation.

Funding This research work is supported by the Intelligent Aerospace Manufacturing (Beijing) Technology Co., Ltd. (SK201901A30-01).

Data Availability No datasets were generated or analysed during the current study.

Declarations

Competing Interests The authors declare no competing interests.

References

1. Alderliesten, R.: Fatigue and fracture of fibre metal laminates. Cham, Switzerland, Vol. 236 Springer (2017). <https://doi.org/10.1007/978-3-319-56227-8>
2. Vlot, A., Gunnink, J.W.: Fibre Metal Laminates: An Introduction. Springer Science & Business Media. Delft, Netherlands (2011)
3. Sherkatghanad, E., Lang, L., Blala, H., Li, L., Alexandrov, S.: Fiber Metal Laminate Structure, a good replacement for monolithic and composite materials. in IOP Conference Series: Materials Science and Engineering IOP Publishing. (2019). <https://doi.org/10.1088/1757-899X/576/1/012034>
4. Jiang, S., Gao, L., Xie, B., Li, K., Wu, C.: Open-Hole Tensile Behavior and Progressive damage of Hybrid Fiber Metal laminates. *Appl. Compos. Mater.* **29**, 547–563 (2022). <https://doi.org/10.1007/s10443-021-09981-0>
5. Etri, H.E., Korkmazet, M.E., Gupta, M.K., Gunay, M., Xu, L.: A state-of-the-art review on mechanical characteristics of different fiber metal laminates for aerospace and structural applications. *Int. J. Adv. Manuf. Technol.* **123**(9), 2965–2991 (2022). <https://doi.org/10.1007/s00170-022-10277-1>
6. Ankush, P.S., Sanan, H.K., Rajesh, K., Venkitanarayanan, P.: Effect of through thickness metal layer distribution on the low velocity impact response of fiber metal laminates. *Polym. Test.* **65**, 301–312 (2018). <https://doi.org/10.1016/j.polymertesting.2017.12.001>
7. Yue, B., Xu, Y., Zhang, W.A.: Novel topology optimization of the Frame Mold for Composite Autoclave process. *Appl. Compos. Mater.* **29**, 2343–2365 (2022). <https://doi.org/10.1007/s10443-022-10068-7>
8. Jakubczak, P.A., Bienias, J., Mania, R., Majerski: Forming of thin-walled profiles made of FML in autoclave process. *Aircr. Eng. Aerosp. Technol.* **90**(3), 506–514 (2018). <https://doi.org/10.1108/AEAT-01-2016-0016>
9. Gisario, A.: Laser forming of glass laminate aluminium reinforced epoxy (GLARE): On the role of mechanical, physical and chemical interactions in the multi-layers material. *Opt. Lasers Eng.* **110**, 364–376 (2018). <https://doi.org/10.1016/j.optlaseng.2018.06.013>
10. Trzepieciński, T., Najm, S.M., Pepelnjak, T., Bensaid, K., Szpunar, M.: Incremental sheet forming of metal-based composites used in aviation and automotive applications. *J. Compos. Sci.* **6**(10), 295 (2022). <https://doi.org/10.3390/jcs6100295>
11. Li, H., Wang, H., Alderliesten, R., Xiang, J., Lin, Y., Xu, Y., et al.: The residual stress characteristics and mechanical behavior of shot peened fiber metal laminates based on the aluminium-lithium alloy. *Compos. Struct.* **254**, 112858 (2020). <https://doi.org/10.1016/j.compstruct.2020.112858>
12. Li, L., Lang, L., Blala, H., Alexandrov, S., Li, S.: The influence of different compositions of fiber metal laminates on the fracture in the semi-solidified stamping forming. *Int. J. Damage Mech.* **31**(8), 1254–1270 (2022). <https://doi.org/10.1177/1056789520954475>
13. Ding, Z., Wang, H., Luo, J., Li, N.: A review on forming technologies of fibre metal laminates. *Int. J. Lightweight Mater. Manuf.* **4**(1), 110–126 (2021). <https://doi.org/10.1016/j.ijlmm.2020.06.006>
14. Kruse, M., Ben Khalifa, N.: Influencing Parameters in the Deep Drawing of Fiber Metal Laminates with Low Viscous Matrix. in International Conference on the Technology of Plasticity. Springer (2023). https://doi.org/10.1007/978-3-031-40920-2_14
15. Heggemann, T., Sapli, H.: Experimental and Numerical Investigations into the Influence of the Process Parameters During the Deep Drawing of Fiber Metal Laminates. in Forming the Future: Proceedings of the 13th International Conference on the Technology of Plasticity. Springer (2021). https://doi.org/10.1007/978-3-030-75381-8_219
16. Li, L., Lang, L., Blala, H., Alexandrov, S.: Formability Analysis of Fiber Metal Laminates with different core and skin layers by stamping process. In materials Science Forum. Trans Tech Publ.((2020). <https://doi.org/10.4028/www.scientific.net/MSF.982.85>
17. Wang, X., Jiang, X., Wang, H., et al.: Manifold learning-assisted uncertainty quantification of system parameters in the fiber metal laminates hot forming process. *J. Intell. Manuf.* (2024). <https://doi.org/10.1007/s10845-024-02343-0>


18. Sanan, H.K., Ankush, P.S., Rajesh, K., Venkitanarayanan, P.: Effect of metal layer placement on the damage and energy absorption mechanisms in aluminium/glass fibre laminates. *Int. J. Imp Eng.* **119**, 14–25 (2018). <https://doi.org/10.1016/j.ijimpeng.2018.04.011>
19. Zhang, Q., Sun, F., Ma, Y., Sun, Z.: The experimental study on the Mechanical properties of Fiber-Reinforced Metal laminates using an innovative heat-solid Integrated Forming Technology. *Metals*. **13**, 1199 (2023). <https://doi.org/10.3390/met13071199>
20. Bigot, N., Guzman-Maldonado, E., Boutaous, M., et al.: A coupled Thermo-mechanical Modelling Strategy based on alternating Direction Implicit Formulation for the Simulation of Multilayered CFRTP Thermo-stamping process. *Appl. Compos. Mater.* **29**, 2321–2341 (2022). <https://doi.org/10.1007/s10443-022-10064-x>
21. Mosse, L., Compston, P., Cantwell, W.J., Cardew-Hall, M., Kalyanasundaram, S.: The effect of process temperature on the formability of polypropylene based fibre–metal laminates. *Compos. Part A: Appl. Sci. Manuf.* **36**(8), 1158–1166 (2005). <https://doi.org/10.1016/j.compositesa.2005.01.009>
22. Weiss, M., Dingle, M.E., Rolfe, B.F., Hodgson, P.D.: The influence of temperature on the forming behavior of metal/polymer laminates in sheet metal forming (2007). <https://doi.org/10.1115/1.2772329>
23. Dou, X., Malingam, S.D., Nam, J., Kalyanasundaram, D.: Finite element modeling of stamp forming process on thermoplastic-based fiber metal laminates at elevated temperatures. *World J. Eng. Technol.* **3**(3), 253–258 (2015). <https://doi.org/10.4236/wjet.2015.33C037>
24. Zal, V., Naeini, H.M., Bahramian, A.R., Sinke, J.: Investigation of the effect of temperature and layup on the press forming of polyvinyl chloride-based composite laminates and fiber metal laminates. *Int. J. Adv. Manuf. Technol.* **89**, 207–217 (2017). <https://doi.org/10.1007/s00170-016-9075-5>
25. Nestler, D., et al.: Continuous film stacking and thermoforming process for hybrid CFRP/aluminum laminates. *Procedia Cirp.* **66**, 107–112 (2017). <https://doi.org/10.1016/j.procir.2017.03.221>
26. Wollmann, T., Hahn, M., Wiedemann, S., Zeiser, A., Jaschinski, J., et al.: Thermoplastic fibre metal laminates: Stiffness properties and forming behaviour by means of deep drawing. *Archives Civil Mech. Eng.* **18**(2), 442–450 (2018). <https://doi.org/10.1016/j.acme.2017.09.001>
27. Wang, J., Li, J., Fu, C., Zhang, G., Zhu, W., Li, X., Yanagimoto, J.: Study on influencing factors of bending springback for metal fiber laminates. *Compos. Struct.* **261**, 113558 (2021). <https://doi.org/10.1016/j.compstruct.2021.113558>
28. Harhash, M., Fischer, T., Grubenmann, M., Hua, W., Heingärtner, J., et al.: Top-hat crashboxes of thermoplastic fibre-metal-laminates processed in one-step thermoforming: Experimental and numerical study. *Compos. Part. B: Eng.* **226**, 109367 (2021). <https://doi.org/10.1016/j.compositesb.2021.109367>
29. Lu, Y., Li, Y., Zhang, Y., Dong, L.: Manufacture of Al/CF/PEEK curved beams by hot stamping forming process. *Mater. Manuf. Processes.* **37**(14), 1597–1609 (2022). <https://doi.org/10.1080/10426914.2022.2032140>
30. Harhash, M., Hua, W., Ziegmann, G., Palkowski, H.: Warm forming of thermoplastic fibre metal laminates. *Mater. Res. Proc.* **25**, 439–446 (2023). <https://doi.org/10.21741/9781644902417-54>
31. Khalid, M., Al Rashid, A., Sheikh, M.: Effect of anodizing process on inter laminar shear strength of GLARE composite through T-peel test: Experimental and numerical approach. *Exp. Tech.* **45**(2), 227–235 (2021). <https://doi.org/10.1007/s40799-020-00433-1>
32. Li, L., Lang, L., Hamza, B., et al.: Effect of hydroforming process on the formability of fiber metal laminates using semi-cured preparation. *Int. J. Adv. Manuf. Technol.* **107**, 3909–3920 (2020). <https://doi.org/10.1007/s00170-020-05281-2>
33. Zhang, M., Mirza, H.A., Zhang, Y.C., Tabasum, M.N., Lang, H., Zou, P.Z.: Investigation into a comprehensive forming limit curve considering multi-parameters effects for semi-cured FMLs through uniform pressure loading test. *Int. J. Damage Mech.* **32**(2), 289–317 (2023). <https://doi.org/10.1177/10567895221135054>
34. Tabasum, M.N., Lang, L., Mirza, H.H., Meng, Z., Blala, H.: Numerical and experimental investigations on the effects of variable cavity pressure on the formability of GLARE using hydromechanical deep drawing. *Int. J. Adv. Manuf. Technol.* **119**(9), 6091–6101 (2022). <https://doi.org/10.1007/s00170-021-08518-w>
35. Mirza, H.A., Lang, L., Tabasum, M.N., Meng, Z., Alexandrov, S., Jiang, J.: An investigation into the Forming of Fiber Metal laminates with different thickness metal skins using Hydromechanical Deep drawing. *Appl. Compos. Mater.* **29**, 1349–1365 (2022). <https://doi.org/10.1007/s10443-022-10024-5>
36. Johnson, G.R.: A constitutive model and data for metals subjected to large strains, high strain rates and high temperatures. in *Proceedings of the 7th International Symposium on Ballistics*, The Hague, Netherlands, (1983)
37. Hashin, Z., Rotem, A.: A fatigue failure criterion for fiber reinforced materials. *J. Compos. Mater.* **7**(4), 448–464 (1973). <https://doi.org/10.1177/002199837300700404>
38. Hashin, Z.: Fatigue failure criteria for unidirectional fiber composites. *J. Appl. Mech.* **47**(4), 329–334 (1980). <https://doi.org/10.1115/1.3157744>

39. Xiao, H., Sultan, M.T.H., Shahar, F.S., Gaff, M., Hui, D.: Recent developments in the mechanical properties of hybrid fiber metal laminates in the automotive industry: A review. *Reviews Adv. Mater. Sci.* **62**(1), 20220328 (2023). <https://doi.org/10.1515/rams-2022-0328>

Publisher's Note Springer Nature remains neutral with regard to jurisdictional claims in published maps and institutional affiliations.

Springer Nature or its licensor (e.g. a society or other partner) holds exclusive rights to this article under a publishing agreement with the author(s) or other rightsholder(s); author self-archiving of the accepted manuscript version of this article is solely governed by the terms of such publishing agreement and applicable law.

Authors and Affiliations

Hamza Blala¹  · Cheng Pengzhi¹ · Zhang Shenglun^{1,2} · Cheng Gang¹ · Ruan Shangwen^{1,3} · Meng Zhang^{1,4}

✉ Hamza Blala
blala.hamza@yahoo.fr

Cheng Pengzhi
chengpengzhi@hyzzbj.com

Zhang Shenglun
zhangshenglun@hyzzbj.com

Cheng Gang
chenggang@hyzzbj.com

Ruan Shangwen
ruanshangwen@buaa.edu.cn

Meng Zhang
stu_zhangmeng@buaa.edu.cn

¹ Intelligent Aerospace Manufacturing (Beijing) Technology Co., Ltd., Beijing 100080, China

² Beijing Information Science and Technology University, Beijing 100192, China

³ University of Science and Technology Beijing, Beijing 100083, China

⁴ School of Energy and Power Engineering, Beihang University, Beijing 100191, China